Exploring Causal Relationships and Adjustment Timescales of Aerosol-Cloud Interactions in Geostationary Satellite Observations and CAM6 Using Wavelet Phase Coherence Analysis

Xiaoli Zhou[1,2,3] ![ORCID], David Painemal[4,5] ![ORCID], Andrew Gettleman[6] ![ORCID], and Graham Feingold[1] ![ORCID]

[1]Chemical Sciences Laboratory, NOAA, Boulder, CO, USA, [2]Cooperative Institute for Research in Environmental Sciences (CIRES), University of Colorado, Boulder, CO, USA, [3]Department of Physics and Atmospheric Science, Dalhousie University, Halifax, NS, Canada, [4]Science Directorate, NASA Langley Research Center, Hampton, VA, USA, [5]Analytical Mechanics Associates, Hampton, VA, USA, [6]Atmospheric, Climate & Earth Science Division, Pacific Northwest National Laboratory, Richland, WA, USA

Abstract We present for the first time within the cloud physics context, the application of wavelet phase coherence analysis to disentangle counteracting physical processes associated with the lead-lag phase difference between cloud-proxy liquid water path (LWP) and aerosol-proxy cloud droplet number concentration (N_d) in an Eulerian framework using satellite-based observations and climate model outputs. This approach allows us to identify the causality and dominant adjustment timescales governing the correlation between LWP and N_d. Satellite observations indicate a more prevalent positive correlation between daytime LWP and N_d regardless of whether LWP leads or lags N_d. The positive cloud water response, associated with precipitation processes, typically occurs within 1 hr, while the negative response resulting from entrainment drying, usually takes 2–4 hr. CAM6 displays excessively rapid negative responses along with overly strong negative cloud water response and insufficient positive response, leading to a more negative correlation between LWP and N_d compared to observations.

Plain Language Summary We employ a wavelet phase coherence analysis to understand how changes in cloud water and cloud droplet concentration are related to each other over time. By analyzing satellite data and climate model output, we study when one variable leads or lags the other and how quickly they adjust to one another. Our findings show that during the day cloud water and cloud droplet concentration often change in the same direction, indicating cloud development and precipitation processes. This effect usually happens within 1 hr. Sometimes cloud water and cloud droplet concentration can change in opposite directions. This is due to clouds being more prone to evaporation at their tops when there is an increase in smaller droplets. Typically this effect takes approximately 2–4 hr to occur. We also compared our observations with a climate model, which shows a too rapid and overly strong negative cloud water response to the change in cloud droplet concentration.

1. Introduction

Warm liquid clouds are known to respond to aerosols via changes in cloud droplet number concentration (N_d) and size (Twomey, 1974), as well as in cloud macroscopic properties such as liquid water path (LWP) or cloud fraction (CF) (Albrecht, 1989; Gryspeerdt et al., 2019; Xue et al., 2008). These responses have a notable impact on the Earth's energy budget; in fact, uncertainty in the current anthropogenic forcing of climate stems primarily from the uncertainty associated with cloud responses to aerosol, as reported in the Sixth Assessment Report of the Intergovernmental Panel on Climate Change (Forster et al., 2021). The uncertainty in cloud water adjustments driven by aerosol perturbations is mainly the consequence of two competing effects: the suppression of precipitation (Albrecht, 1989) that increases cloud liquid water path (LWP), and evaporation-entrainment feedbacks where the increase in N_d promotes increasing entrainment rates and evaporation efficiency, consequently decreasing LWP (Ackerman et al., 2004; Bretherton et al., 2007; Wang et al., 2003).

A common approach to estimating cloud water adjustments to aerosol is to examine the statistical relationships between LWP and an aerosol-proxy N_d, in LWP-N_d space (Gryspeerdt et al., 2019; Hoffmann et al., 2020; Zhou & Feingold, 2023), and by computing the slope of their linear regression ($L_0 = \frac{dln(LWP)}{dln(Nd)}$; Qiu et al., 2023; Zhang

et al., 2022). Recently, Mülmenstädt et al. (2024) found that statistical LWP-N_d correlation in unperturbed general circulation models (GCMs) shows an opposite sign compared to the cloud water response in perturbed-aerosol GCM simulations (Gryspeerdt et al., 2020), suggesting that these correlations may not be causally linked.

While causality is easier to establish in model experiments, it is challenging in observations (Christensen et al., 2021; Mülmenstädt et al., 2024), particularly those based on snapshots from polar-orbiting satellites. Fons et al. (2023) built a physics-informed causal graph and computed LWP-N_d correlation based on the graph path rule to disentangle counteracting physical processes and remove confounding influences. However, this approach is limited by its reliance on the initial assumptions made in constructing the causal graphs. Moreover, there is a lack of thorough evaluation of aerosol-cloud interaction (ACI) adjustment timescales in GCMs, impeding further improvements in the representation of ACI in GCMs for reliable assessment of aerosol indirect radiative forcing. A recent study by Glassmeier et al. (2021) found that the timescale for negative cloud water adjustment due to the evaporation-entrainment feedbacks is ~20hr in large eddy simulations—much longer compared to the very short cloud brightening response (order 15 min) and the positive cloud water adjustment due to precipitation suppression (~90 min; Dagan et al., 2018). An adequate assessment is imperative for a better understanding of aerosol effects on climate.

In this study, we apply for the first time a wavelet phase coherence analysis (Kumar & Foufoula-Georgiou, 1997) to identify the lead-lag causality between LWP and N_d by examining their phase difference in the periods when the two variables are significantly coherent (Torrence & Webster, 1999). Wavelet analysis offers the benefit of capturing both time and frequency (rate of oscillation) localization, making it particularly advantageous for investigating variables that exhibit temporal fluctuations in frequency. A dominant adjustment timescale is identified for each phase (lead-lag) scenario that corresponds to specific physical processes. We apply this analysis to daytime satellite cloud retrievals derived from the Spinning Enhanced Visible and Infrared Imager (SEVIRI) and Community Atmospheric Model, version 6 (CAM6) daytime clouds. Our study offers an innovative approach to exploring the causality and adjustment timescales of ACI in observations and GCMs. In addition to providing important insights into LWP adjustments, this method can help to discern the imprint of microphysical parameterizations across different GCMs and facilitate GCM intercomparison studies.

2. Data and Methodology

We analyze 2 months (June-August 2018) of single-layer liquid phase low level (<3 km) cloud properties (LWP and N_d) over the North Atlantic Ocean (26ºN 50ºN; 45ºW 15ºW) using the National Aeronautics and Space Administration (NASA) Langley Research Center (LaRC) cloud properties derived from SEVIRI on Meteosat-11 and from simulations performed using CAM6 (Bogenschutz et al., 2018; Gettelman et al., 2019)—the atmospheric component of Version 2 of the Earth System Model (Danabasoglu et al., 2020). The 3-month data is considered sufficient to reliably convey the result, as similar outcomes were observed with 1-month dataset (figure not shown). The summer season is chosen because of the notable prevalence of boundary layer clouds (Dong et al., 2014, 2023; Rémillard et al., 2012).

2.1. SEVIRI

SEVIRI cloud products are retrieved using the LaRC's ClOud and Radiation Property retrieval System (Sat-CORPS) algorithms (e.g., Painemal et al., 2021; Qiu et al., 2024), with a spatial resolution of 3 km at nadir and a 15 min temporal resolution. LaRC's LWP is computed following Minnis et al. (2011) as $LWP = \frac{4 r_e \tau}{3 Q_{ext}}$, where Q_{ext} represents the drop extinction efficiency and is assumed equal to 2. N_d is calculated as a function of $\left(\frac{\tau}{r_e^5}\right)^{\frac{1}{2}}$ following Grosvenor et al., 2018, with the adiabatic fraction assumed to be 0.8 (Albrecht et al., 1990; Brenguier et al., 2011; Wood & Taylor, 2001; Zuidema et al., 2012). LWP and N_d are considered as nearly independent due to the near-independent retrieving nature of τ and r_e retrievals (Nakajima & King, 1990), with LWP and N_d primarily covarying with τ and r_e, respectively. Note that given the retrieval reliance on visible/near-infrared satellite channels, the cloud microphysical properties cannot be reliably estimated during nighttime. To minimize uncertainties associated with bias in satellite cloud microphysics retrievals, we only select pixels with $\tau \geq 3$, and $r_e \geq 3$ µm. We recognize the potential scattering geometry biases (e.g., Várnai & Marshak, 2007). While Smalley & Lebsock, 2023 (SL23) offer a lookup table for correcting LWP geometry, it is designed for nonprecipitating conditions and is not tailored to the specific SEVIRI geometry and pixel resolution. Moreover, the correction in

SL23 is not directly applicable to our dataset, because SatCORPS algorithms rely on different spectral channels for the derivation of τ and r_e than those used in SL23. Given the uncertainties in the SL23 method we use the uncorrected LWP but limit our analysis to pixels with a solar zenith angle (SZA) < 65° (Painemal, 2018; Painemal et al., 2013; Qiu et al., 2023). Lastly, given that the instrument viewing zenith angle for the region of study is less than 50°, we effectively minimize viewing geometry effects and remove severe pixel coarsening at the edge of the scan (e.g., Maddux et al., 2010). Although LWP and N_d are calculated based on different profiles of water content, we view this as a minor concern compared to the uncertainties in actual cloud adiabaticity, cloud base temperature, and pressure that are required for the retrieval of N_d.

2.2. CAM6 Nudged-Wind Simulations

The CAM6 simulations in this study are run with prescribed climatological forcing. A finite-volume dynamical core of 0.9° longitude x 1.25° latitude resolution is used with 32 vertical levels and a model time step of 30 min.

We conduct CAM6 simulations using two different microphysics packages. C-MG2 refers to a simulation conducted with the two-moment bulk microphysics scheme described in Gettelman and Morrison (2015). C-ML refers to a simulation conducted with a bin-bulk microphysics scheme that employs a machine learning emulator to efficiently replicate the results of a bin microphysics model with low computational cost (Gettelman et al., 2021). To assess the model's performance over short periods, an additional C-MG2-dt5 is run with a model time step of 5 min.

To facilitate model evaluation against satellite observations, CAM6 was run in a nudged configuration using the NASA Modern-Era Retrospective analysis for Research and Applications version 2 (MERRA-2; Molod et al., 2015; Rienecker et al., 2011) horizontal winds with a relaxation time scale of 24 hr. Consistent with the observational analysis, only daytime simulation data with SZA < 65° are used.

2.3. 1D Wavelet Analysis

We divide the domain (26ºN 50ºN; 45ºW 15ºW) into 25 scenes of 2° × 2° each in SEVIRI and 180 scenes in CAM6. Note that in SEVIRI, we only select the central 25 scenes within the domain, as these areas are minimally affected by the distortion in the satellite images. Figure S1 in Supporting Information S1 shows the SEVIRI domain and the 25 selected scenes. In each 2° × 2° scene, we apply a 1D wavelet analysis to the time series of scene-average LWP and N_d of the cloudy pixels in both SEVIRI and CAM6.

Taking advantage of the ability of wavelet analysis to capture both time and frequency localization, we apply a 1D discrete wavelet transform as a band-pass filter bank in time to segregate the time series of LWP and N_d into fluctuations at different octave frequency bands (frequency bands where the upper frequency limit is equal to twice the lower frequency limit), $2^n \times dt \times (2^{-1/2} – 2^{1/2})$, where n is the number of the frequency band ($n = 1, 2, 3...$), and dt is the temporal resolution of the data. We refer to these octaves by the weighted averages of their frequency ranges $2^n \times dt$. For SEVIRI, with a temporal resolution of 15 min, LWP and N_d are segregated into 5 octave bands: 30 min, 1 hr, 2 hr, 4 hr, and 8 hr. For C-MG and C-ML with a temporal resolution of 30 min, the corresponding octave bands are 1, 2, 4, and 8 hr. For C-MG2-dt5 with a temporal resolution of 5 min, the octave bands are 10, 20, 40, 80, 160, and 320 min. This decomposition allows us to analyze cloud water adjustment slopes at different time scales.

To determine the phase difference between LWP and N_d, we further allocate 12 smaller frequency intervals within each octave frequency band (hereafter sub-octave bands). In each sub-octave band, we use the standard Morlet wavelet, which is a Gaussian modulated sine wave of the form used by Torrence and Compo (1998), and apply the wavelet coherence transform (WCT) to the normalized LWP and N_d to locate the time, frequency, and phase (lead-lag) where LWP and N_d co-vary. The normalization is achieved by subtracting the 3 month mean, and dividing by the standard deviation. In each frequency octave band, we select the periods when LWP and N_d are both significantly coherent (based on Monte Carlo simulations with a 95% confidence level) in at least one sub-octave band and exceed five time steps in duration. These periods are defined as *coherent periods* at a specific frequency octave. To ensure that the coherent periods reflect the local cloud evolution rather than clouds advected from outside of the scene, we remove from the analysis those scenes with a daily mean horizontal wind speed greater than 6 m s^{-1}. The phase difference (0–360°) between LWP and N_d for each coherent period is determined based on an average of phase differences across all sub-octave bands. The phase difference represents the angular
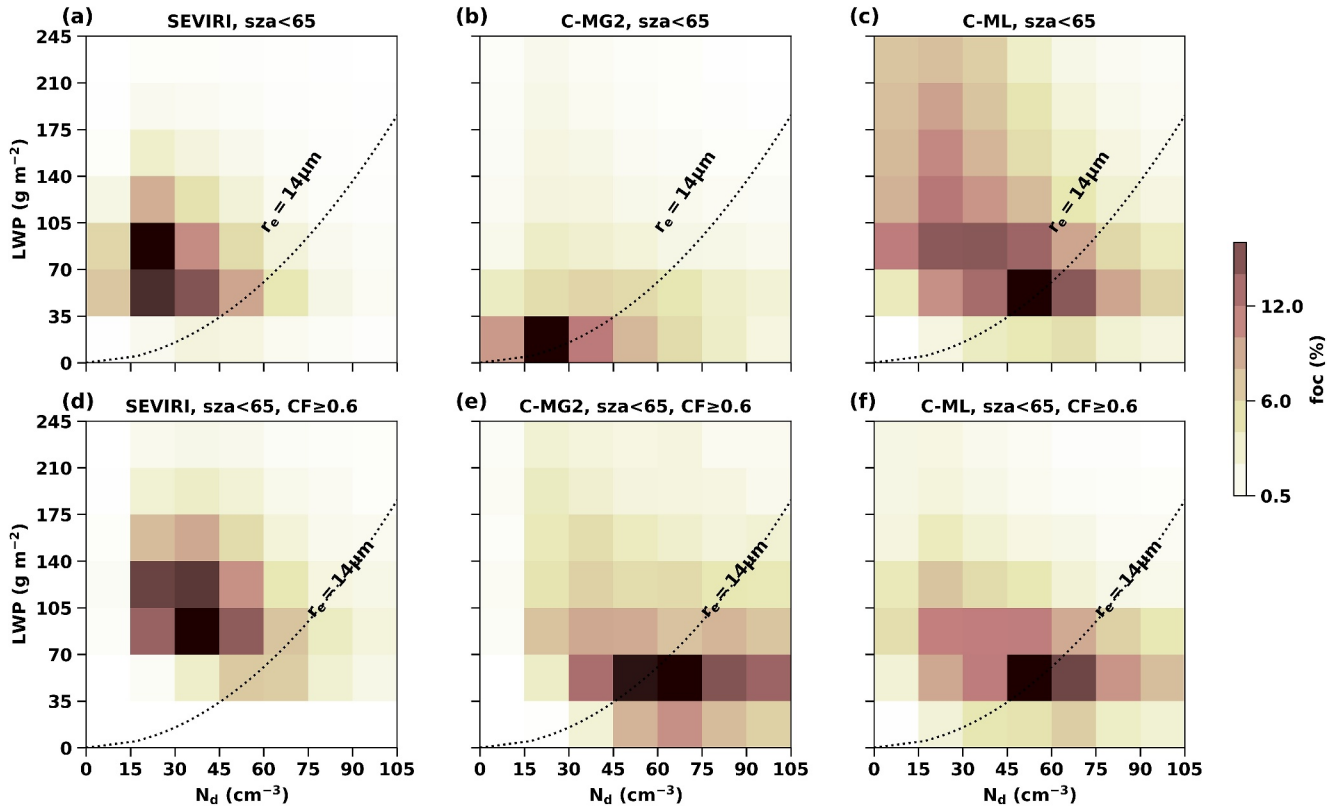
Figure 1. Frequency of occurrence of daytime (SZA < 65°) cloud properties in the LWP- N_d space for (a) SEVIRI, (b) C-MG2, and (c) C-ML. (d)–(f) are for stratocumulus clouds (CF ≥ 0.6). The black dashed lines correspond to an adiabatic volume-mean droplet radius at cloud top of 14 μm (adiabatic condensation rate of 2.14×10^6 kg m^{-4}) following Glassmeier et al. (2019). The LWP and N_d bin sizes are 35 g m^{-2} and 15 cm^{-3} respectively.

offset in the wavelet transform between LWP and N_d, illustrating the extent to which one signal leads or lags the other.

The coherent periods are grouped into four scenarios based on phase difference values:

Scenario I (LWP^+N_d): LWP positively leads N_d, defined as when LWP leads N_d by less than 90°. This scenario can occur due to cloud development or dissipation when cloud development leads to more activation of cloud droplets and vice versa. Additionally, precipitation washout of cloud water and droplets can lead to Scenario I in which case the decrease in LWP and N_d occurs as a consequence of precipitation reaching the surface.

Scenario II (LWP^-N_d): LWP negatively leads N_d, defined as when LWP leads N_d by more than 90° but less than 180°. This scenario describes an increasing LWP from vertical cloud development leading to a reduced N_d through the collision-coalescence process or rain removal of N_d (precipitation scavenging).

Scenario III (N_d^+LWP): N_d positively leads LWP, defined as when LWP lags N_d by less than 90°. This scenario may arise from an increase in LWP due to the suppression of collision-coalescence and precipitation in response to increasing N_d.

Scenario IV (N_d^-LWP): N_d negatively leads LWP, defined as when LWP lags N_d by more than 90° but less than 180°. This scenario reflects entrainment drying driven by N_d as a result of the evaporation-entrainment feedbacks.

3. Results

3.1. Cloud Properties From SEVIRI and CAM6

Figures 1a–1c show the 2d histograms of LWP and N_d for SEVIRI, C-MG2, and C-ML during the daytime (SZA < 65°). Clouds are observed most frequently at LWP ~70 g m^{-2} and $N_d \sim 20$ cm^{-3}, and are mostly precipitating ($r_e > 14$ μm; left of the $r_e = 14$ μm isoline). Clouds in C-MG2 are too thin compared to SEVIRI; they are improved

in C-ML, although N_d in C-ML is larger and more scattered. The LWP-N_d distribution of C-MG2-dt5 closely resembles that of C-MG2 (not shown).

Figures 1d–1f show the 2d histograms for stratocumulus clouds, which we define as clouds with cloud fraction (CF) greater than 0.6 (60%). In the rest of the paper, unless stated otherwise, we will focus on stratocumulus clouds. The observed stratocumulus clouds occur most frequently at LWP ~ 100 g m^{-2} and $N_d \sim 30$ cm^{-3} and are likely drizzling. The cloud distribution in the LWP-N_d space closely resembles that shown in Qiu et al. (2023) who used 4 years of SEVIRI retrievals for the month of July over the Eastern North Atlantic, supporting the representativeness of our 3 month data. We observe a discernible increase in N_d for thinner clouds where drizzle is likely inhibited (i.e., negative correlation between LWP and N_d). Both C-MG2 and C-ML tend to underestimate stratocumulus LWP while overestimating N_d, although C-ML exhibits a slight improvement. This result indicates a higher occurrence of non-precipitating clouds in CAM6 compared to SEVIRI.

3.2. Linear Regression Slopes Between LWP and N_d in SEVIRI and CAM6

Computing the linear regression slope $L_0 = \mathrm{dln}\,(\mathrm{LWP})/\mathrm{dln}\,(N_d)$ from the LWP-N_d distribution illustrated in Figure 1 yields -0.12, -0.35, -0.45, and -0.29 for SEVIRI, C-MG2-dt5, C-MG2 and C-ML. This result indicates a much stronger decrease in LWP with an increase in N_d in CAM6 compared to observations.

Among the three simulations, C-ML L_0 more closely aligns with that of SEVIRI whereas L_0 in C-MG2 is much more negative. When the model time step is reduced to 5 min (C-MG2-dt5), L_0 slightly increases and better matches that of SEVIRI. This underscores the importance of high temporal resolution in improving the representation of cloud-aerosol interactions.

The L_0 values computed from the LWP-N_d distribution are commonly considered as a proxy for cloud water adjustment to aerosol, yet they only reflect correlation and do not prove causality. To gain insights into causality and to identify the timescales and L_0s caused by specific physical processes, we now examine the coherent periods of LWP and N_d and their corresponding phase difference in Sections 3.3 and 3.4.

3.3. The Occurrence of Phase Scenarios Between LWP and N_d

In total, there are 1,139, 1,352, 573, and 832 coherent periods respectively for SEVIRI, C-MG2-dt5, C-MG2, and C-ML. We divide the coherent periods of LWP and N_d into the four phase scenarios based on the phase relationship between LWP and N_d (Section 2): LWP positively and negatively leads N_d (I and II); N_d positively and negatively leads LWP (III and IV). Examples of the four scenarios are included in Figure S2 in Supporting Information S1.

We first examine the occurrence of coherent periods of LWP and N_d for each phase scenario across different octave frequency bands (colored bars in Figure 2, left y-axis). For a better comparison between SEVIRI and CAM6, we only show their shared octave frequency bands of 1, 2, 4, and 8 hr. For C-MG2-dt5, we present the 40, 80, 160, and 320 min octave bands instead computed from its 5 min temporal resolution (Section 2.3). Results from SEVIRI show that positive scenarios consistently exhibit a higher occurrence than negative scenarios across octaves. The positive scenarios occur more frequently at shorter octaves, while the negative scenarios do not exhibit significant occurrence until the 2 hr octave. This suggests that negative scenarios typically take longer to occur compared to positive scenarios. The negative scenarios are associated with processes like evaporation-entrainment feedbacks and precipitation scavenging (as discussed in Section 2.3), both of which take time to impart their influence on the boundary layer compared to the cloud development and collision-coalescence suppression processes linked to the positive scenarios.

Consistent with SEVIRI, positive scenarios in CAM6 simulations generally occur more frequently than negative scenarios, and their occurrence decreases at longer frequency octaves. However, in all three CAM6 simulations, negative scenarios are equally or more frequent at octaves shorter than 2 hr than at longer octaves, suggesting that negative scenarios tend to occur too rapidly in CAM6. This is particularly notable in the scenario of N_d negatively leading LWP (scenario IV), characterized by the presence of evaporation-entrainment feedbacks (Section 2). We hypothesize that this bias is related to the long-standing issue in the representation of parameterizations of turbulence and microphysics, irrespective of microphysics scheme and model timestep. That being said, reducing the model time step (C-MG2-dt5) tends to increase the occurrence of coherent periods, especially positive scenarios. The bin-bulk microphysics scheme (C-ML) also tends to show a higher occurrence of positive coherent periods
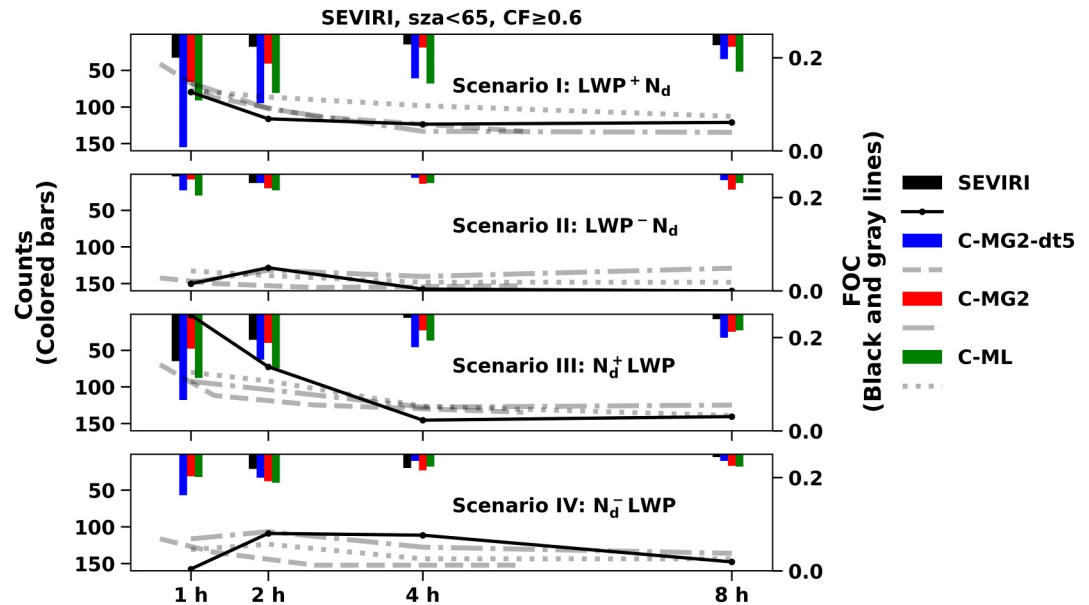
Figure 2. The total counts (lines; right *y*-axis) and the frequency of occurrence (colored bars; left *y*-axis) of coherent periods of LWP and N_d for daytime (SZA <65°) stratocumulus clouds (CF ≥ 0.6) for scenarios I-IV at octave frequency bands of 1 hr, 2 hr, 4 hr, and 8 hr in SEVIRI, C-MG2, and C-ML, and at octave frequency bands of 40 min, 80 min, 160 min, and 320 min in C-MG2-dt5. For better visualization, the total counts of C-MG2-dt5 are plotted at the same octave bands as SEVIRI.

compared to the bulk microphysics scheme (C-MG2). A higher occurrence of positive coherent periods in C-MG2-dt5 and C-ML could help to mitigate the overly strong negative statistics-based L_0 shown in Section 3.2.

Figure 2 also shows the corresponding frequency of occurrence of coherent periods of LWP and N_d across octave bands for each scenario for SEVIRI and CAM6 simulations (black and gray lines; right *y*-axis). Here we define the *dominant adjustment timescale* (τ_{adj}) of each scenario as the octave band of the highest frequency of occurrence. For SEVIRI, this translates to τ_{adj} values of ≤1, 2, ≤1, and 2–4 hr for scenarios I-IV. Note that the τ_{adj} of the positive scenarios may be shorter than 1 hr if one considers shorter octaves. Compared to SEVIRI, CAM6 simulations show consistent τ_{adj} for positive scenarios, but there is a noticeable bias in the τ_{adj} of negative scenarios, especially the scenario where N_d negatively leads LWP (scenario IV), where CAM 6 suggests a much shorter τ_{adj} (<1 hr), implying that the entrainment-evaporation feedbacks occur too rapidly in CAM6. Another notable aspect is that although CAM6 simulations show a typical τ_{adj} of 1 hr or less for the scenario of N_d positively leading LWP (Scenario III), this timescale is less dominant compared to SEVIRI, suggesting that the precipitation suppression in CAM6 does not occur fast enough, irrespective of model timestep and microphysics scheme. This is consistent with scenario II (LWP negatively leads N_d), where both C-ML and C-MG2 show a noticeable frequency of occurrence at 4 and 8 hr octave bands, implying a delayed precipitation scavenging process. The fast negative and slow positive scenarios in CAM6 could also contribute to the more negative statistics-based L_0 in CAM6 discussed in Section 3.2.

3.4. Regression Slopes Between LWP and Nd for the Four Phase Scenarios

We now calculate the regression slopes (L_0) between LWP and N_d for each scenario. To establish a stronger connection of L_0 with physical processes, here we calculate L_0 at the dominant adjustment timescales for each scenario ($L_{\tau_{adj}}$) (i.e., 1, 2, 1, and 2–4 hr for scenarios I-IV) for SEVIRI and CAM6 runs. $L_{\tau_{adj}}$ provides direct insight into the process-driven LWP and N_d adjustments. For scenario I (LWP^+N_d), $L_{\tau_{adj}}$ signifies the positive adjustment of cloud droplet number concentration to cloud water changes via cloud development or precipitation washout of LWP and N_d. For scenario II (LWP^-N_d), $L_{\tau_{adj}}$ depicts the reduction in cloud droplet number concentration in response to cloud water increase through precipitation scavenging. For scenario III (N_d^+LWP), $L_{\tau_{adj}}$ describes the increase in cloud water resulting from elevated aerosol levels due to precipitation suppression. For scenario IV
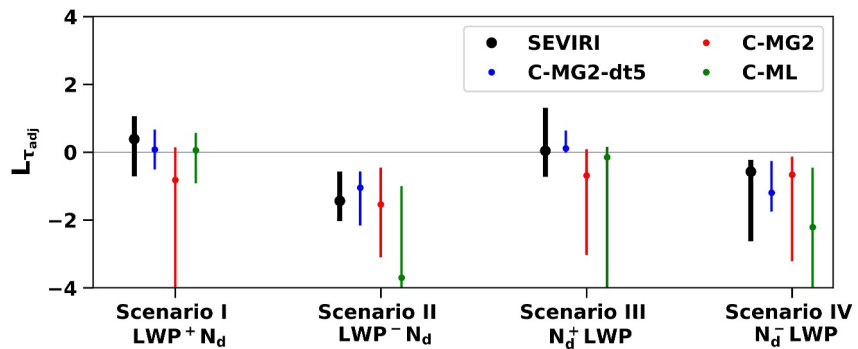
Figure 3. The adjustment slopes at the dominant adjustment timescale $L_{\tau_{adj}}$ for daytime (SZA < 65°) stratocumulus clouds (CF ≥ 0.6) for scenarios I–IV. In SEVIRI, C-MG2, and C-ML, the dominant adjustment timescales are 1 hr, 2 hr, 1 hr, and 2–4 hr for Scenarios I-IV In C-MG2-dt5, they are calculated at 160 min, 40 min, 40 min, and 80 min.

(N_d^-LWP), $L_{\tau_{adj}}$ represents negative cloud water adjustment to aerosols due to evaporation-entrainment feedbacks. We refer readers to Section 2.3 for the details on the links between scenarios and physical meanings. As shown in Figure 3, the median $L_{\tau_{adj}}$ for SEVIRI are 0.4, −1.4, 0.04, −0.6, for scenarios I-IV. The sign of $L_{\tau_{adj}}$ generally aligns with the scenarios (i.e., negative scenarios exhibit negative $L_{\tau_{adj}}$ and vice versa). Negative scenarios (i.e., scenarios II and IV), which take longer to occur, tend to have more significant magnitude than positive scenarios (i.e., scenarios I and III). The scenario-based $L_{\tau_{adj}}$ of negative scenarios (i.e., −1.4 for scenario II and −0.6 for scenario IV) show more pronounced slopes, compared to the statistic-based L_0 value of −0.12 (as implied by the correlation slope in the LWP-N_d space in Figure 1 and quantified in Section 3.2), likely because the statistic-based L_0 dilutes signals of opposing signs.

The adjustment slopes in CAM6 diverge from SEVIRI in several aspects: the bulk microphysics scheme is associated with overly weak positive responses of N_d and LWP, suggesting the inefficiency in precipitation suppression (Scenario III N_d^+LWP) and precipitation washout of LWP and N_d (Scenario I LWP^+N_d), as well as cloud development in C-MG2, thereby contributing to a more negative statistic-based L_0. This bias is noticeably improved with the bin-bulk microphysics scheme or with a shorter model timestep. On the other hand, the bin-bulk microphysics scheme appears to underperform when it comes to the negative responses related to precipitation scavenging and entrainment-evaporation feedbacks, resulting in overly negative responses. Figures S3 and S4 in Supporting Information S1 show our findings after adjusting for LWP using the lookup table from SL23. The results closely resemble those presented in Figures 2 and 3.

4. Discussion and Conclusion

In this study, we apply a one-dimensional wavelet phase coherence analysis to analyze local temporal evolution of daytime cloud liquid water path (LWP) and cloud droplet number concentration (N_d), considered as a proxy for the aerosol embedded in the cloud field, based on SEVIRI retrievals and CAM6 simulations. We study the dominant adjustment timescale (τ_{adj}) governing the coherent period between LWP and N_d from SEVIRI in four lead-lag phase scenarios, defined based on the phase difference between LWP and N_d. This approach effectively disentangles LWP adjustments due to the counteracting physical processes of precipitation suppression and entrainment-evaporation feedbacks on fast and slow timescales respectively.

SEVIRI features a more prevalent positive correlation between daytime LWP and N_d, with less occurrence of negative correlation, in both lead-lag instances where LWP leads or lags N_d. In the context of aerosol-cloud interaction, we focus on N_d-led scenarios (N_d^+LWP and N_d^-LWP). The positive cloud water response due to collision-coalescence suppression (N_d^+LWP) is found to be more rapid (within 1 hr) than the negative cloud water response resulting from entrainment drying (N_d^-LWP) which usually takes 2–4 hr (Figure 2). Although less frequent, the negative cloud water response features a greater adjustment magnitude (Figure 3), contributing to an overall negative correlation between LWP and N_d (Figure 1).

Compared to SEVIRI, CAM6 simulations show a more negative correlation between LWP and N_d for their daytime clouds (Figure 1). Our wavelet analysis suggests that this might result from excessively rapid negative

responses along with overly strong negative cloud water adjustments and insufficient positive adjustments in CAM6 (Figures 2 and 3). Overall the bin-bulk microphysics scheme performs better than the bulk microphysics scheme in terms of statistical correlations between LWP and N_d and positive cloud water adjustment, but the evaporation-entrainment feedbacks (N_d^-LWP) is stronger than that inferred from SEVIRI, highlighting the need for improvements in the parameterizations of turbulence and microphysics. The bulk microphysics scheme presents insufficient positive scenarios related to precipitation suppression and the corresponding cloud water adjustment is too weak, indicating the scheme's deficiency in representing precipitation. This is notably improved with a shorter model timestep, which shows a more similar LWP-N_d distribution compared to SEVIRI (Figure 1). This suggests that a shorter model timestep can, to some extent, overcome the precipitation parameterization deficiency. We thereby recommend using short model timesteps for addressing aerosol-cloud interaction problems. Nonetheless, CAM6 shows agreement with SEVIRI in several aspects, including a higher prevalence of positive scenarios and comparable τ_{adj} for positive scenarios. Nighttime clouds in CAM6 show comparable τ_{adj} to daytime values (Figure S5 in Supporting Information S1). We defer comprehensive analysis of nighttime clouds to future studies due to a lack of nighttime observations.

With its easy application to satellite and GCM model output, the wavelet phase coherence analysis has the potential not only to provide insights into τ_{adj} in geostationary satellite-based observations, but also to identify biases in τ_{adj} and the slope of aerosol-cloud interactions between GCMs resulting from different treatments of complex microphysical, turbulence, and radiation parameterizations and their coupling. As such it presents another opportunity for assessing GCMs using geostationary satellite-based measurements as a reference. Although this study focuses on the Eulerian framework, the method can also be applied to the Lagrangian, flow-following framework. More broadly, this method can be applied to any two collocated variables to study their causal relationship.

Data Availability Statement

The processed data for all the figures are stored in the following NOAA data archive: https://csl.noaa.gov/groups/csl9/datasets/.

References

Ackerman, A. S., Kirkpatrick, M. P., Stevens, D. E., & Toon, O. B. (2004). The impact of humidity above stratiform clouds on indirect aerosol climate forcing. *Nature*, *432*(7020), 1014–1017. https://doi.org/10.1038/nature03174

Albrecht, B. A. (1989). Aerosols, cloud microphysics, and fractional cloudiness. *Science*, *245*(4923), 1227–1230. https://doi.org/10.1126/science.245.4923.1227

Albrecht, B. A., Fairall, C. W., Thomson, D. W., White, A. B., Snider, J. B., & Schubert, W. H. (1990). Surface-based remote sensing of the observed and the adiabatic liquid water content of stratocumulus clouds. *Geophysical Research Letters*, *17*(1), 89–92. https://doi.org/10.1029/gl017i001p00089

Bogenschutz, P. A., Gettelman, A., Hannay, C., Larson, V. E., Neale, R. B., Craig, C., & Chen, C. C. (2018). The path to CAM6: Coupled simulations with CAM5. 4 and CAM5. 5. *Geoscientific Model Development*, *11*(1), 235–255. https://doi.org/10.5194/gmd-11-235-2018

Brenguier, J. L., Burnet, F., & Geoffroy, O. (2011). Cloud optical thickness and liquid water path–does the k coefficient vary with droplet concentration? *Atmospheric Chemistry and Physics*, *11*(18), 9771–9786. https://doi.org/10.5194/acp-11-9771-2011

Bretherton, C. S., Blossey, P. N., & Uchida, J. (2007). Cloud droplet sedimentation, entrainment efficiency, and subtropical stratocumulus albedo. *Geophysical Research Letters*, *34*(3). https://doi.org/10.1029/2006gl027648

Christensen, M., Gettelman, A., Cermak, J., Dagan, G., Diamond, M., Douglas, A., & Yuan, T. (2021). Opportunistic experiments to constrain aerosol effective radiative forcing. *Atmospheric Chemistry and Physics Discussions*, *2021*, 1–60.

Dagan, G., Koren, I., Kostinski, A., & Altaratz, O. (2018). Organization and oscillations in simulated shallow convective clouds. *Journal of Advances in Modeling Earth Systems*, *10*(9), 2287–2299. https://doi.org/10.1029/2018ms001416

Danabasoglu, G., Lamarque, J. F., Bacmeister, J., Bailey, D. A., DuVivier, A. K., Edwards, J., et al. (2020). The community earth system model version 2 (CESM2). *Journal of Advances in Modeling Earth Systems*, *12*(2), e2019MS001916. https://doi.org/10.1029/2019ms001916

Dong, X., Xi, B., Kennedy, A., Minnis, P., & Wood, R. (2014). A 19-month record of marine aerosol–cloud–radiation properties derived from DOE ARM mobile facility deployment at the Azores. Part I: Cloud fraction and single-layered MBL cloud properties. *Journal of Climate*, *27*(10), 3665–3682. https://doi.org/10.1175/jcli-d-13-00553.1

Dong, X., Zheng, X., Xi, B., & Xie, S. (2023). A climatology of midlatitude maritime cloud fraction and radiative effect derived from the ARM ENA ground-based observations. *Journal of Climate*, *36*(2), 531–546. https://doi.org/10.1175/jcli-d-22-0290.1

Fons, E., Runge, J., Neubauer, D., & Lohmann, U. (2023). Stratocumulus adjustments to aerosol perturbations disentangled with a causal approach. *npj Climate and Atmospheric Science*, *6*(1), 130. https://doi.org/10.1038/s41612-023-00452-w

Forster, P., Storelvmo, T., Armour, K., Collins, W., Dufresne, J.-L., Frame, D., et al. (2021). The Earth's energy budget, climate feedbacks, and climate sensitivity. In V. Masson-Delmotte, P. Zhai, A. Pirani, S. L. Connors, C. Péan, S. Berger, et al. (Eds.), *Climate change 2021: The physical science basis. Contribution of working group I to the Sixth assessment Report of the intergovernmental Panel on climate change* (pp. 923–1054). Cambridge University Press. https://doi.org/10.1017/9781009157896.009

Gettelman, A., Gagne, D. J., Chen, C. C., Christensen, M. W., Lebo, Z. J., Morrison, H., & Gantos, G. (2021). Machine learning the warm rain process. *Journal of Advances in Modeling Earth Systems*, *13*(2), e2020MS002268. https://doi.org/10.1029/2020ms002268

Gettelman, A., Hannay, C., Bacmeister, J. T., Neale, R. B., Pendergrass, A. G., Danabasoglu, G., et al. (2019). High climate sensitivity in the community earth system model version 2 (CESM2). *Geophysical Research Letters*, *46*(14), 8329–8337. https://doi.org/10.1029/2019gl083978

Gettelman, A., & Morrison, H. (2015). Advanced two-moment bulk microphysics for global models. Part I: Off-line tests and comparison with other schemes. *Journal of Climate*, *28*(3), 1268–1287. https://doi.org/10.1175/jcli-d-14-00102.1

Glassmeier, F., Hoffmann, F., Johnson, J. S., Yamaguchi, T., Carslaw, K. S., & Feingold, G. (2019). An emulator approach to stratocumulus susceptibility. *Atmospheric Chemistry and Physics*, *19*(15), 10191–10203. https://doi.org/10.5194/acp-19-10191-2019

Glassmeier, F., Hoffmann, F., Johnson, J. S., Yamaguchi, T., Carslaw, K. S., & Feingold, G. (2021). Aerosol-cloud-climate cooling overestimated by ship-track data. *Science*, *371*(6528), 485–489. https://doi.org/10.1126/science.abd3980

Grosvenor, D. P., Sourdeval, O., Zuidema, P., Ackerman, A., Alexandrov, M. D., Bennartz, R., et al. (2018). Remote sensing of droplet number concentration in warm clouds: A review of the current state of knowledge and perspectives. *Review*, *56*(2), 409–453. https://doi.org/10.1029/2017rg000593

Gryspeerdt, E., Goren, T., Sourdeval, O., Quaas, J., Mülmenstadt, J., Dipu, S., et al. (2019). Constraining the aerosol influence on cloud liquid water path. *Atmospheric Chemistry and Physics*, *19*(8), 5331–5347. https://doi.org/10.5194/acp-19-5331-2019

Gryspeerdt, E., Mülmenstädt, J., Gettelman, A., Malavelle, F. F., Morrison, H., Neubauer, D., et al. (2020). Surprising similarities in model and observational aerosol radiative forcing estimates. *Atmospheric Chemistry and Physics*, *20*(1), 613–623. https://doi.org/10.5194/acp-20-613-2020

Hoffmann, F., Glassmeier, F., Yamaguchi, T., & Feingold, G. (2020). Liquid water path steady states in stratocumulus: Insights from process-level emulation and mixed-layer theory. *Journal of the Atmospheric Sciences*, *77*(6), 2203–2215. https://doi.org/10.1175/JAS-D-19-0241.1

Kumar, P., & Foufoula-Georgiou, E. (1997). Wavelet analysis for geophysical applications. *Reviews of Geophysics*, *35*(4), 385–412. https://doi.org/10.1029/97rg00427

Maddux, B. C., Ackerman, S. A., & Platnick, S. (2010). Viewing geometry dependencies in MODIS cloud products. *Journal of Atmospheric and Oceanic Technology*, *27*(9), 1519–1528. https://doi.org/10.1175/2010JTECHA1432.1

Minnis, P., Sun-Mack, S., Young, D. F., Heck, P. W., Garber, D. P., Chen, Y., et al. (2011). CERES edition-2 cloud property retrievals using TRMM VIRS and terra and aqua MODIS data—Part I: Algorithms. *IEEE Transactions on Geoscience and Remote Sensing*, *49*(11), 4374–4400. https://doi.org/10.1109/tgrs.2011.2144601

Molod, A., Takacs, L., Suarez, M., & Bacmeister, J. (2015). Development of the GEOS-5 atmospheric general circulation model: Evolution from MERRA to MERRA2. *Geoscientific Model Development*, *8*(5), 1339–1356. https://doi.org/10.5194/gmd-8-1339-2015

Mülmenstädt, J., Gryspeerdt, E., Dipu, S., Quaas, J., Ackerman, A. S., Fridlind, A. M., et al. (2024). General circulation models simulate negative liquid water path–droplet number correlations, but anthropogenic aerosols still increase simulated liquid water path. *EGUsphere*, *2024*(12), 1–29. https://doi.org/10.5194/acp-24-7331-2024

Nakajima, T., & King, M. D. (1990). Determination of the optical thickness and effective particle radius of clouds from reflected solar radiation measurements. Part I: Theory. *Journal of the Atmospheric Sciences*, *47*(15), 1878–1893. https://doi.org/10.1175/1520-0469(1990)047<1878:dotota>2.0.co;2

Painemal, D. (2018). Global estimates of changes in shortwave low-cloud albedo and Fluxes due to variations in cloud droplet number concentration derived from CERES-MODIS satellite sensors. *Geophysical Research Letters*, *45*(17), 9288–9296. https://doi.org/10.1029/2018gl078880

Painemal, D., Minnis, P., & Sun-Mack, S. (2013). The impact of horizontal heterogeneities, cloud fraction, and liquid water path on warm cloud effective radii from CERES-like Aqua MODIS retrievals. *Atmospheric Chemistry and Physics*, *13*(19), 9997–10003. https://doi.org/10.5194/acp-13-9997-2013

Painemal, D., Spangenberg, D., Smith Jr, W. L., Minnis, P., Cairns, B., Moore, R. H., et al. (2021). Evaluation of satellite retrievals of liquid clouds from the GOES-13 imager and MODIS over the midlatitude North Atlantic during the NAAMES campaign. *Atmospheric Measurement Techniques*, *14*(10), 6633–6646. https://doi.org/10.5194/amt-14-6633-2021

Qiu, S., Zheng, X., Painemal, D., Terai, C., & Zhou, X. (2023). Diurnal variation of aerosol indirect effect for warm marine boundary layer clouds in the eastern north Atlantic. *EGUsphere*, *2023*, 1–30.

Qiu, S., Zheng, X., Painemal, D., Terai, C. R., & Zhou, X. (2024). Daytime variation in the aerosol indirect effect for warm marine boundary layer clouds in the eastern North Atlantic. *Atmospheric Chemistry and Physics*, *24*(5), 2913–2935. https://doi.org/10.5194/acp-24-2913-2024

Rémillard, J., Kollias, P., Luke, E., & Wood, R. (2012). Marine boundary layer cloud observations in the Azores. *Journal of Climate*, *25*(21), 7381–7398. https://doi.org/10.1175/jcli-d-11-00610.1

Rienecker, M. M., Suarez, M. J., Gelaro, R., Todling, R., Bacmeister, J., Liu, E., et al. (2011). MERRA: NASA's modern-era retrospective analysis for research and applications. *Journal of climate*, *24*(14), 3624–3648.

Smalley, K. M., & Lebsock, M. D. (2023). Corrections for geostationary cloud liquid water path using microwave imagery. *Journal of Atmospheric and Oceanic Technology*, *40*(9), 1049–1061. https://doi.org/10.1175/jtech-d-23-0030.1

Torrence, C., & Compo, G. P. (1998). A practical guide to wavelet analysis. *Bulletin of the American Meteorological Society*, *79*(1), 61–78. https://doi.org/10.1175/1520-0477(1998)079<0061:apgtwa>2.0.co;2

Torrence, C., & Webster, P. J. (1999). Interdecadal changes in the ENSO–monsoon system. *Journal of Climate*, *12*(8), 2679–2690. https://doi.org/10.1175/1520-0442(1999)012<2679:icitem>2.0.co;2

Twomey, S. J. A. E. (1974). Pollution and the planetary albedo. *Atmospheric Environment*, *8*(12), 1251–1256. 1967. https://doi.org/10.1016/0004-6981(74)90004-3

Várnai, T., & Marshak, A. (2007). View angle dependence of cloud optical thicknesses retrieved by Moderate Resolution Imaging Spectroradiometer (MODIS). *Journal of Geophysical Research*, *112*(D6). https://doi.org/10.1029/2005jd006912

Wang, S., Wang, Q., & Feingold, G. (2003). Turbulence, condensation, and liquid water transport in numerically simulated nonprecipitating stratocumulus clouds. *Journal of the Atmospheric Sciences*, *60*(2), 262–278. https://doi.org/10.1175/1520-0469(2003)060<0262:tcalwt>2.0.co;2

Wood, R., & Taylor, J. P. (2001). Liquid water path variability in unbroken marine stratocumulus cloud. *Quarterly Journal of the Royal Meteorological Society*, *127*(578), 2635–2662. https://doi.org/10.1256/smsqj.57806

Xue, H., Feingold, G., & Stevens, B. (2008). Aerosol effects on clouds, precipitation, and the organization of shallow cumulus convection. *Journal of the Atmospheric Sciences*, *65*(2), 392–406. https://doi.org/10.1175/2007JAS2428.1

Zhang, J., Zhou, X., Goren, T., & Feingold, G. (2022). Albedo susceptibility of northeastern pacific stratocumulus: The role of covarying meteorological conditions. *Atmospheric Chemistry and Physics*, *22*(2), 861–880. https://doi.org/10.5194/acp-22-861-2022

Zhou, X., & Feingold, G. (2023). Impacts of mesoscale cloud organization on aerosol-induced cloud water adjustment and cloud brightness. *Geophysical Research Letters*, *50*(13), e2023GL103417. https://doi.org/10.1029/2023gl103417

Zuidema, P., Leon, D., Pazmany, A., & Cadeddu, M. (2012). Aircraft millimeter-wave passive sensing of cloud liquid water and water vapor during VOCALS-REx. *Atmospheric Chemistry and Physics*, *12*(1), 355–369. https://doi.org/10.5194/acp-12-355-2012